Range-Division Multiplexing for MIMO OFDM Joint Radar and Communications

Oliver Lang, *Member, IEEE*, Christian Hofbauer, *Member, IEEE*, Reinhard Feger, and Mario Huemer, *Senior Member, IEEE*

***Abstract*—An orthogonal frequency-division multiplexing (OFDM) waveform enables simultaneous radar sensing and communications. In the multiple-input multiple-output (MIMO) case with several transmit (Tx) antennas, multiplexing the transmit signals is usually implemented using equidistant subcarrier interleaving (ESI), thus allowing the separation of the transmit signals in frequency domain. In this work, a multiplexing technique denoted as range-division multiplexing (RDMult) is analyzed, which allows separating signals radiated by different Tx antennas along the range axis of a range-Doppler map. This work also investigates the effects of RDMult on the communication task. It turns out that RDMult heavily distorts the channel statistics by introducing a repetitive pattern of deep fading holes, which severely distort the transmission of data. To combat this issue, this work proposes a communication system especially designed for RDMult, including methods for data estimation, channel estimation and synchronization. Simulations confirm the effectiveness of these concepts in terms of bit error ratio (BER) performance.**

***Index Terms*—Communication, MIMO, Multiplexing, OFDM Radar, Radar.**

I. Introduction

JOINT radar sensing and communication systems are a field of intensive research. Possible future applications include automotive radar sensing and car-to-car communication [1], [2], [3], [4], [5]. Orthogonal frequency-division multiplexing (OFDM) is a prominent waveform candidate for such systems [6], [7], [8], [9], [10], [11], [12], [13], [14], [15], [16]. Usually, multiple-input multiple-output (MIMO) radar systems with multiple transmit (Tx) and receive (Rx) antennas in combination with digital beamforming (DBF) are employed for detecting the angular positions of objects. This requires multiplexing of the signals radiated by different Tx antennas such that they become separable in the receiver. Some possible multiplexing techniques are discussed in [15], [16], [17], [18], [19], [20], [21], [22], [23], [24], [25], [26]. For joint radar and communications, the most popular multiplexing technique is equidistant subcarrier interleaving (ESI) [15], [24]. For ESI, the subcarriers are equidistantly allocated to the Tx antennas such that a subcarrier is transmitted on a single Tx antenna only, as exemplarily shown in Fig. 1 a).

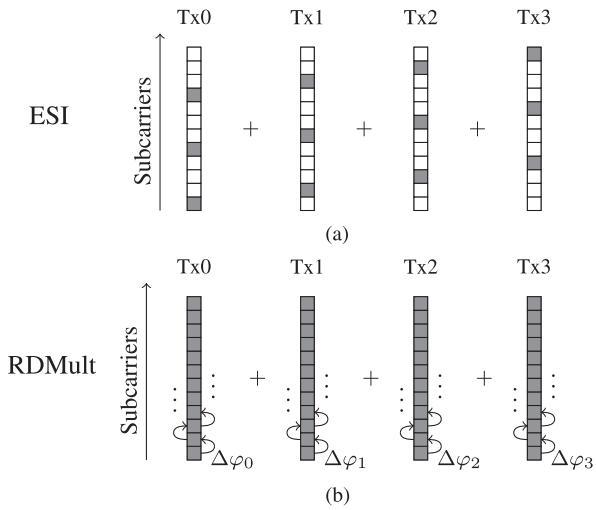

Fig. 1. a) Schematic sketch of the subcarrier allocation for ESI for the case of 4 Tx antennas. Only a fraction of the available subcarriers are active at the Tx antennas (gray blocks). b) Schematic sketch of the principle of RDMult. Here, all subcarriers are active at every Tx antenna. A phase shift $\Delta\varphi_k$, with k denoting the Tx antenna index, is applied from subcarrier to subcarrier. This causes a shift of the received signals along the range axis in the RDM.

Extensions of ESI based on non-equidistantly allocated subcarriers and randomly allocated subcarriers are investigated in [16] and [25], respectively. Both approaches employ computationally expensive compressed sensing (CS) methods. A further extension with dynamic allocation of the subcarriers is presented in [26]. Unfortunately, this method comes with an increased noise floor.

A multiplexing technique denoted as auto-correlation-based code-division multiplexing (AC-CDM) is proposed in [22]. This multiplexing technique transmits the same data on all Tx antennas and on all subcarriers but with unique time delays

Manuscript received 4 April 2022; revised 15 July 2022; accepted 20 August 2022. Date of publication 31 August 2022; date of current version 16 January 2023. The work of Christian Hofbauer was supported by the Silicon Austria Labs (SAL), owned by the Republic of Austria, the Styrian Business Promotion Agency (SFG), the Federal State of Carinthia, the Upper Austrian Research (UAR), and the Austrian Association for the Electric and Electronics Industry (FEEI). This work was supported by the "University SAL Labs" Initiative of SAL and its Austrian partner universities for applied fundamental research for electronic based systems. The review of this article was coordinated by Dr. Haijun Zhang. *(Corresponding author: Oliver Lang.)*

Oliver Lang is with the Institute of Signal Processing, Johannes Kepler University, 4040 Linz, Austria (e-mail: oliver.lang@jku.at).

Christian Hofbauer is with the Silicon Austria Labs GmbH, 4040 Linz, Austria (e-mail: christian.hofbauer@silicon-austria.com).

Reinhard Feger is with the Institute for Communications Engineering and RF-Systems, Johannes Kepler University, 4040 Linz, Austria (e-mail: Reinhard.Feger@jku.at).

Mario Huemer is with the JKU LIT SAL eSPML Lab, 4040 Linz, Austria (e-mail: mario.huemer@jku.at).

Digital Object Identifier 10.1109/TVT.2022.3203205

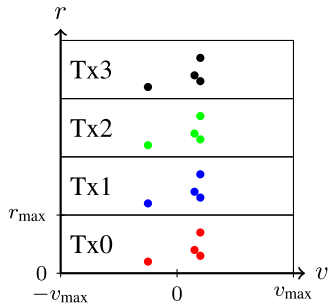

Fig. 2. Range-Doppler map for RDMult. The dots represent objects that appear $N_{\text{Tx}} = 4$ times.

(implemented via phase rotations in the frequency domain). These time delays shift the corresponding receive signals along the range axis in the range-Doppler map (RDM), resulting in N_{Tx} peaks in the RDM for each real object. Here, N_{Tx} denotes the number of Tx antennas. In the receiver, the time delays are undone for each Tx antenna, still one observes $N_{\text{Tx}} - 1$ ambiguous peaks for each main peak along the range axis of the RDM. However, by choosing irregular time delays, one can identify the ambiguous peaks in the receiver.

Another interesting multiplexing technique is investigated in [23], which also shifts the signal components radiated by different Tx antennas within the RDM. This is achieved by transmitting the same data on all Tx antennas and on all subcarriers, and in addition, employing a discrete Fourier transform (DFT) matrix as precoding matrix. This precoding matrix shifts the corresponding receive signals along the range and/or the velocity axis of the RDM. In the receiver, the signal components belonging to a specific Tx antenna can then be isolated by inspecting only the corresponding area in the RDM.

This work focuses on a multiplexing technique denoted as range-division multiplexing (RDMult).[1] This multiplexing technique shares some similarities with AC-CDM and with the approach in [23], however, there exist some distinct differences in the details and in the focus of the analysis as discussed later. The working principle of RDMult is sketched in Fig. 1 b). RDMult for MIMO OFDM radar systems is achieved by applying a phase shift $\Delta\varphi_k$ from subcarrier to subcarrier at the transmitter, with $k = 0, \ldots, N_{\text{Tx}} - 1$ denoting the Tx antenna index. This phase shift causes a shift of the received signal along the range axis in the RDM. In the receiver, a separation of signal components transmitted by different transmit antennas is simply achieved by slicing the RDM along the range axis. This yields separated measurements for every transmit-receive antenna pair. A possible RDM is sketched in Fig. 2 for an exemplary set of $N_{\text{Tx}} = 4$ transmit antennas. This RDM is split up into N_{Tx} blocks along the range axis, each one belonging to a specific Tx antenna.

As will be shown, the radar performance of a MIMO OFDM radar system employing RDMult is comparable to that of a MIMO OFDM radar system using ESI in terms of the signal-to-noise ratio (SNR).

In this work, a detailed analysis of the implications of RDMult on the communication task is carried out. This analysis will show that activating all subcarriers at each Tx antenna in every OFDM symbol causes a subcarrier-dependent constructive or destructive interference of the transmitted signals at the communication receiver. This effect is specific to MIMO systems and does not occur in the single-input single-output (SISO) case. It will turn out that for RDMult, these constructive and destructive interferences appear in a cyclic pattern along the subcarriers. Based on a detailed investigation of this effect, this work proposes a joint radar sensing and communication system especially designed for the use in combination with RDMult. The communication system includes methods for data estimation, channel estimation and synchronization. The performance of the proposed communication system will be investigated via bit error ratio (BER) simulations, which confirm the effectiveness of these methods.

RDMult shares some similarities with AC-CDM proposed in [22]. In fact, the transmit signals coincide when

- choosing the parameter N_{guard} in [22] to be zero, and
- choosing the phase shift according to the design rule discussed in Section IV-A of this work.

Differences between [22] and this work include:

- In [22], the phase rotations applied in the transmitter are undone in the receivers for all Tx-Rx combinations. This increases the computational complexity compared to the approach in this work.
- In contrast to [22], the work at hand contains a comprehensive investigation of the impact of the multiplexing technique on the communication task.

As already stated, RDMult is also related to the multiplexing technique investigated in [23], which shifts the signal components radiated by different Tx antennas along both dimensions of the RDM. The precoding matrix employed in [23] can be translated to a phase shift from subcarrier to subcarrier as utilized in this work. It will be shown, that the design rule for choosing the phase shift in [23] differs from the one proposed in this work (cf. Section IV-A). Moreover, the effects of this phase shift on the communication task were not analyzed in [23].

This paper is organized as follows: Section II recaps the basics of the OFDM waveform. Section III presents the derivation of the multiplexing technique RDMult. A communication setup utilizing this technique is proposed in Section V, and the performance analyzed based on BER simulations in Section VI. Finally, Section VII concludes this work.

Notation: Lower-case bold face variables ($\mathbf{a}$, $\mathbf{b}$,...) indicate vectors, and upper-case bold face variables ($\mathbf{A}$, $\mathbf{B}$,...) indicate matrices. We further use $\mathbb{R}$ and $\mathbb{C}$ to denote the set of real- and complex-valued numbers, respectively, $(\cdot)^T$ to denote transposition, $(\cdot)^H$ to denote conjugate transposition, and $(\cdot)^*$ to denote complex conjugation. $\mathbf{I}^n$ denotes the identity matrix of size $n \times n$, and $\mathbf{0}^{n\times m}$ denotes the zero matrix of size $n \times m$. $\mathbf{1}^n$ indicates a column vector of length n with all elements being one. $\oslash$ represents the Hadamard division, and j represents the imaginary unit.

II. Basics of OFDM Radar

At first, an overall description of the SISO OFDM waveform and the standard signal processing chain for radar applications is provided. Next, a detailed mathematical description of the

[1]The abbreviation RDMult is chosen in order to prevent any confusion with the range-Doppler map, which is usually abbreviated as RDM.

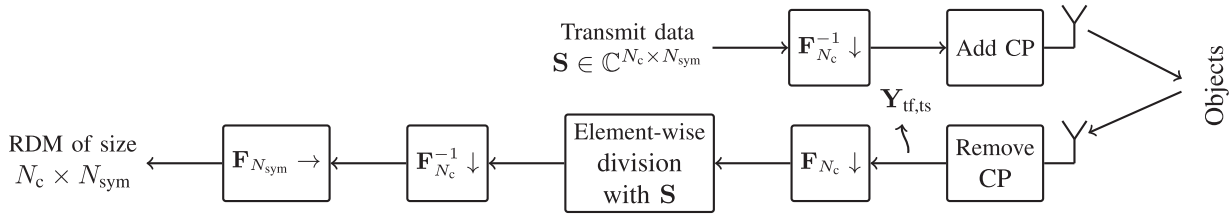

Fig. 3. Visualization of the standard SISO OFDM radar signal processing. The analog front-end, the ADC, and the parallel-to-serial conversion are not shown for the sake of brevity. The arrows $\downarrow$ / $\rightarrow$ indicate that the corresponding operation is applied on the columns/rows of a matrix, respectively.

SISO signal model is presented. This SISO signal model is then extended to the MIMO case.

A. OFDM Waveform and Radar Signal Processing

The transmit signal of the OFDM waveform consists of orthogonal subcarriers [27]. The complex-valued amplitudes of these subcarriers may contain the transmit information in form of subcarrier symbols, e.g., quadrature phase-shift keying (QPSK) symbols. In this work, the term subcarrier symbol is used as a general expression for the complex-valued amplitudes of the subcarriers. Dedicated realizations of these subcarrier symbols in form of e.g., data symbols or pilot symbols are discussed later in Section V.

In the following, $\mathbf{F}_N \in \mathbb{C}^{N \times N}$ denotes the DFT matrix of size $N \times N$. The number of subcarriers is denoted as N_c, and the number of consecutively transmitted OFDM symbols is given by N_sym.

The basic OFDM radar signal processing chain for the SISO case is shown in Fig. 3. The matrix $\mathbf{S} \in \mathbb{C}^{N_\mathrm{c} \times N_\mathrm{sym}}$ contains the transmit subcarrier symbols, where each row represents a subcarrier, and each column represents an OFDM symbol in the frequency domain. The time domain OFDM symbols are obtained via inverse discrete Fourier transform (IDFT) operations applied on the columns of $\mathbf{S}$. These time domain OFDM symbols are extended with a cyclic prefix (CP) of length T_cp, modulated with the carrier frequency f_c, and radiated via a Tx antenna. The bandwidth B of the radiated signals is given by $B = N_\mathrm{c}\Delta f$, where Δf denotes the subcarrier spacing.

The received signal consists in general of multiple reflections of the transmitted signal. After removing the CP in complex baseband (BB), the remaining samples of an OFDM symbol are transformed into the frequency domain via a DFT. This step yields the received subcarrier symbols. After an element-wise division with the transmit subcarrier symbols, the distance information is extracted by applying the so-called range IDFT along the subcarriers.

A relative velocity of an object causes a phase shift from OFDM symbol to OFDM symbol. Hence, the velocity information can be recovered by applying the so-called Doppler DFT along the N_sym OFDM symbols. This processing step yields the desired RDM of size $N_\mathrm{c} \times N_\mathrm{sym}$.

The RDM features the following performance measures [8], [12]: the range resolution Δr, the maximum unambiguous range r_max, the velocity resolution Δv, and the maximum unambiguous relative velocity v_max. These performance measures are given by

$$\Delta r = \frac{c_0}{2B} \qquad \Delta v = \frac{c_0}{2 f_\mathrm{c} N_\mathrm{sym} \left(T + T_\mathrm{cp}\right)} \tag{1}$$

$$r_\mathrm{max} = \Delta r N_\mathrm{c} \qquad v_\mathrm{max} = \pm \Delta v \frac{N_\mathrm{sym}}{2}, \tag{2}$$

where c_0 is the speed of light, and $T = 1/\Delta f$ is the duration of one OFDM symbol. It is worth noting that the processing gain for the described radar signal processing chain is given by $G_\mathrm{p} = N_\mathrm{sym} N_\mathrm{c}$.

B. MIMO Signal Model

In the following, we briefly introduce the mathematical description of the MIMO signal model, which is based on the model derived in [13]. The reader is referred to [13] for further details and discussions. The MIMO signal model is developed for multiplexing techniques in general and is not limited to RDMult or ESI. The description starts with the case of one Rx antenna. The extension to several Rx antennas is discussed later on.

Let N_path denote the number of propagation paths between the Tx antennas and the Rx antenna. Each one features a delay equal to the round-trip delay time of the path. A relative velocity along a propagation path causes a Doppler shift, which is accounted for in the mathematical model by including the effect of inter-carrier interference (ICI) and by including a phase rotation from OFDM symbol to OFDM symbol. Note that this phase rotation is usually referred to as common phase error (CPE) in the communications society. Since the effects of the Doppler shift are accounted for by ICI and by the CPE, the round-trip delay times are approximated time-independent and given by $\tau_{i,k} = 2 r_{i,k}/c_0$, where $0 \leq i < N_\mathrm{path}$ is the index of a propagation path, and where $0 \leq k < N_\mathrm{Tx}$. $r_{i,k}$ denotes the propagation distance of the ith path and of the kth Tx antenna.

In the following, $\mathbf{D}_N(f)$ denotes a diagonal matrix defined as

$$\mathbf{D}_N(f) = \begin{bmatrix} 1 & 0 & \dots & 0 \\ 0 & \mathrm{e}^{\mathrm{j}2\pi f} & \dots & 0 \\ \vdots & \vdots & \ddots & \vdots \\ 0 & 0 & \dots & \mathrm{e}^{\mathrm{j}2\pi f (N-1)} \end{bmatrix} \in \mathbb{C}^{N \times N}, \tag{3}$$

where f is a unitless place-holder variable. The analog-to-digital converter (ADC) samples at the receiver after removing the CP are stored in the matrix $\mathbf{Y}_{\text{tf,ts}} \in \mathbb{C}^{N_\text{c} \times N_\text{sym}}$, where 'tf' and 'ts' stand for fast time and slow time, respectively. Each column represents one time domain OFDM symbol. When neglecting additive measurement noise, the matrix $\mathbf{Y}_{\text{tf,ts}}$ is given by [13] as

$$\mathbf{Y}_{\text{tf,ts}} = \sum_{k=0}^{N_\text{Tx}-1} \sum_{i=0}^{N_\text{path}-1} \bar{a}_{i,k} \mathbf{D}_{N_\text{c}} \left(\frac{\bar{f}_{\text{D}_i}}{N_\text{c}} \right) \mathbf{F}_{N_\text{c}}^{-1} \mathbf{D}_{N_\text{c}}^{*}(\bar{\tau}_{i,k}) \cdot \mathbf{S}_k \mathbf{D}_{N_\text{sym}}(\bar{f}_{\text{D}_i} \alpha). \tag{4}$$

where

$$\bar{f}_{\text{D}_i} = -2 v_i f_\text{c} / (c_0 \Delta f) \tag{5}$$

is referred to as normalized Doppler frequency [13], and where v_i denotes the relative velocity for the ith path. $\bar{\tau}_{i,k} = \tau_{i,k} \Delta f$ denote normalized time delays, and $\alpha = (T + T_\text{cp})/T = 1 + \Delta f T_\text{cp}$ is a factor that incorporates the overhead caused by the CP relative to the duration of an OFDM symbol.

The subcarrier symbols for each Tx antenna in the frequency domain are stored in the matrices $\mathbf{S}_k \in \mathbb{C}^{N_\text{c} \times N_\text{sym}}$. Matrix $\mathbf{D}_{N_\text{c}}^{*}(\bar{\tau}_{i,k})$ applies a phase rotation caused by the round-trip delay times for each subcarrier. The magnitude and phase changes during propagation are considered via $\bar{a}_{i,k} = a_i \cdot \text{e}^{-\text{j}2\pi f_\text{c} \tau_{i,k}}$. A CPE is modeled by $\mathbf{D}_{N_\text{sym}}(\bar{f}_{\text{D}_i} \alpha)$, and the effects of ICI are modeled by $\mathbf{D}_{N_\text{c}}(\frac{\bar{f}_{\text{D}_i}}{N_\text{c}})$.

As stated in [13], the standard OFDM radar signal processing ignores the ICI term $\mathbf{D}_{N_\text{c}}(\frac{\bar{f}_{\text{D}_i}}{N_\text{c}})$. It is well-known that ICI increases the noise floor in the RDM [13]. In this work, the ICI term is neglected within the mathematical derivations as well, since the noise floor is not the focus of this derivation. However, the ICI term is included in all simulations. A simple inclusion of the ICI term into the derivation would be possible by separating it into two parts: $\mathbf{D}_{N_\text{c}}(\frac{\bar{f}_{\text{D}_i}}{N_\text{c}}) = \mathbf{I}^{N_\text{c}} + (\mathbf{D}_{N_\text{c}}(\frac{\bar{f}_{\text{D}_i}}{N_\text{c}}) - \mathbf{I}^{N_\text{c}})$. For the first part, the normal derivation as presented is valid, while the second part results in an additional noise term.

The incorporation of several Rx antennas can be achieved by constructing a matrix in (4) for every Rx antenna, with a proper adaptation of the parameters $\bar{a}_{i,k}$ and $\bar{\tau}_{i,k}$.

The MIMO signal model in (4) is the foundation of the following derivation of the RDMult technique.

III. Range-Division Multiplexing

In this section, the multiplexing technique for OFDM radars denoted as RDMult will be derived. This technique modifies the transmit subcarrier symbols such that the signals radiated by different Tx antennas can be separated along the range axis within the RDM.

The derivation of RDMult starts with the signal model in (4), where the ICI term $\mathbf{D}_{N_\text{c}}(\frac{\bar{f}_{\text{D}_i}}{N_\text{c}})$ will be neglected as already discussed in Section II. A shift along the range axis in the RDMult at the receiver is achieved by adding a phase shift from one subcarrier to the next one prior to transmission. Let $\Delta\varphi_k$ denote this phase shift for the kth Tx antenna. This means that the first subcarrier of the first Tx antenna remains unaltered,

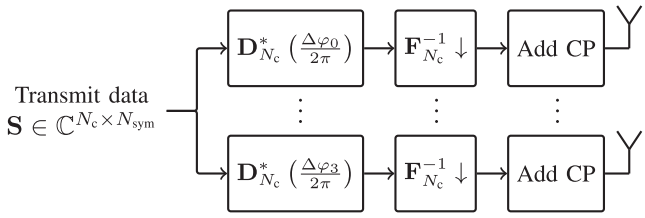

Fig. 4. Visualization of the transmitter signal processing chain for RDMult for $N_\text{Tx} = 4$. The analog front-end and the parallel-to-serial conversion are not shown.

the second subcarrier is rotated by $\Delta\varphi_0$, the third subcarrier is rotated by $2\Delta\varphi_0$, and so on. This procedure is repeated for all Tx antennas and can be mathematically described by defining $\mathbf{S}_k$ in (4) as

$$\mathbf{S}_k = \mathbf{D}_{N_\text{c}}^{*}\left(\frac{\Delta\varphi_k}{2\pi}\right) \mathbf{S}. \tag{6}$$

Matrix $\mathbf{S}$ contains subcarrier symbols, which will be the same for all Tx antennas. Fig. 4 visualizes the basic transmitter signal processing chain for RDMult, including the manipulation in (6), the transformation into the time domain, and the extension of the time domain signals with the CP.

The receiver signal processing chain for RDMult is the same as for SISO OFDM systems shown in Fig. 3. The model describing the receive signal for RDMult after removing the CP is given by inserting (6) into the MIMO signal model in (4). Applying the DFT to recover the received OFDM symbols in frequency domain yields

$$\mathbf{Y}_{\text{f,ts}} = \mathbf{F}_{N_\text{c}} \mathbf{Y}_{\text{tf,ts}} = \sum_{k=0}^{N_\text{Tx}-1} \sum_{i=0}^{N_\text{path}-1} \bar{a}_{i,k} \mathbf{D}_{N_\text{c}}^{*}\left(\frac{\Delta\varphi_k}{2\pi} + \bar{\tau}_{i,k}\right) \mathbf{S} \mathbf{D}_{N_\text{sym}}\left(\bar{f}_{\text{D}_i} \alpha\right). \tag{7}$$

The subscripts 'f' and 'ts' denote the frequency domain and slow time over the first and second matrix dimension, respectively [13]. An element wise division by $\mathbf{S}$ yields

$$\mathbf{Z}_{\text{f,ts}} = \mathbf{Y}_{\text{f,ts}} \oslash \mathbf{S} \tag{8}$$

$$= \sum_{k=0}^{N_\text{Tx}-1} \sum_{i=0}^{N_\text{path}-1} \bar{a}_{i,k} \mathbf{D}_{N_\text{c}}^{*}\left(\frac{\Delta\varphi_k}{2\pi} + \bar{\tau}_{i,k}\right) \cdot \mathbf{1}^{N_\text{c}} (\mathbf{1}^{N_\text{sym}})^T \mathbf{D}_{N_\text{sym}}\left(\bar{f}_{\text{D}_i} \alpha\right)$$

$$= \sum_{k=0}^{N_\text{Tx}-1} \sum_{i=0}^{N_\text{path}-1} \bar{a}_{i,k} \mathbf{d}_{N_\text{c}}^{*}\left(\frac{\Delta\varphi_k}{2\pi} + \bar{\tau}_{i,k}\right) \mathbf{d}_{N_\text{sym}}^{T}\left(\bar{f}_{\text{D}_i} \alpha\right), \tag{9}$$

where the identity $(\mathbf{D}_a \mathbf{M} \mathbf{D}_b) \oslash \mathbf{M} = \mathbf{D}_a \mathbf{1}^n (\mathbf{1}^m)^T \mathbf{D}_b$ was used, which holds for arbitrary matrices $\mathbf{M} \in \mathbb{C}^{n \times m}$ with non-zero elements, and arbitrary diagonal matrices $\mathbf{D}_a \in \mathbb{C}^{n \times n}$ and $\mathbf{D}_b \in \mathbb{C}^{m \times m}$.

For the range IDFT and the Doppler DFT, usually windowed IDFT/DFT operations are applied to reduce the side lobes. The window function of length N shall be stored in a vector $\mathbf{w}_N \in \mathbb{R}^N$, and its ith element shall be denoted as $w_N[i]$. The diagonal

matrix with $\mathbf{w}_N$ on its main diagonal shall be denoted as $\mathbf{W}_N = \text{diag}(\mathbf{w}_N) \in \mathbb{R}^{N\times N}$. Then, applying the windowed range IDFT yields [13]

$$\begin{aligned}\mathbf{Z}_{\text{r,ts}} &= \mathbf{F}_{N_\text{c}}^{-1}\mathbf{W}_{N_\text{c}}\mathbf{Z}_{\text{f,ts}} \\ &= \sum_{k=0}^{N_\text{Tx}-1}\sum_{i=0}^{N_\text{path}-1} \bar{a}_{i,k}\mathbf{u}_{N_\text{c}}^{*}\left(\frac{\Delta\varphi_k}{2\pi}+\bar{\tau}_{i,k}\right)\mathbf{d}_{N_\text{sym}}^{T}\left(\bar{f}_{\text{D}_i}\alpha\right)\end{aligned} \tag{10}$$

with

$$\mathbf{u}_N(f) = \mathbf{F}_N\mathbf{W}_N\mathbf{d}_N(f) \tag{11}$$

$$= \begin{bmatrix} \sum_{n=0}^{N-1} w_N[n]\text{e}^{\text{j}2\pi(f-\frac{0}{N})n} \\ \vdots \\ \sum_{n=0}^{N-1} w_N[n]\text{e}^{\text{j}2\pi(f-\frac{N-1}{N})n}\end{bmatrix} \in \mathbb{C}^N. \tag{12}$$

Finally, applying the windowed Doppler DFT yields

$$\mathbf{Z}_{\text{r,v}} = \mathbf{Z}_{\text{r,ts}}\mathbf{W}_{N_\text{sym}}\mathbf{F}_{N_\text{sym}} \tag{13}$$

$$= \sum_{k=0}^{N_\text{Tx}-1}\sum_{i=0}^{N_\text{path}-1} \bar{a}_{i,k}\mathbf{u}_{N_\text{c}}^{*}\left(\frac{\Delta\varphi_k}{2\pi}+\bar{\tau}_{i,k}\right)\mathbf{u}_{N_\text{sym}}^{T}\left(\bar{f}_{\text{D}_i}\alpha\right), \tag{14}$$

which represents the desired RDM.

IV. Properties of RDMult

In the following, three aspects of RDMult for the radar sensing task are discussed.

A. Choice of $\Delta\varphi_k$

The phase shift $\Delta\varphi_k$ determines how the signal of the kth Tx antenna is mapped along the range axis. For the case of $N_\text{Tx} = 4$ transmit antennas, one can show that the choice of $\Delta\varphi_k = \{0, \frac{\pi}{2}, \pi, \frac{3\pi}{2}\}$ yields 4 equally spaced areas along the range axis as sketched in Fig. 2. Hence, these values represent the primary choice for $\Delta\varphi_k$ in this work. In Appendix A, it is proven that by choosing $\Delta\varphi_k = 2\pi\frac{p}{N_\text{c}}$ for any $p \in \mathbb{Z}$, objects in the RDM are circularly shifted by p range bins. Moreover, this circular shift does not induce any amplitude or phase changes such that the values in the RDM can directly be used for DBF [4], [28], [29].

For some applications, it may be beneficial to vary the values of the phase shift $\Delta\varphi_k$ from RDM to RDM. Possible benefits of doing so is the detection of objects violating the maximum unambiguous range using tracking algorithms. However, such special cases are beyond the scope of this work. Note that a similar approach for detecting objects violating the maximum unambiguous range is not possible for ESI.

The approach in [23] uses a different design rule for the phase shift $\Delta\varphi_k$. There, a DFT matrix is utilized as precoding matrix. In the context of this paper, this precoding matrix can be translated into a phase shift from subcarrier to subcarrier of $\Delta\varphi_k = 2\pi\frac{k}{N_\text{Tx}}$, which not necessarily fulfills the constraint derived in Appendix A. Hence, depending on the choice of N_c and N_Tx, the approach in [23] may introduce distortions of the amplitude and phase values in the RDM.

B. Beampattern

For phased arrays, a phase shift applied from Tx antenna to Tx antenna allows steering the main signal energy towards a specific direction. The average signal energy in a specific direction is quantified by the beampattern, which is usually nonuniform along the angular domain for phased arrays. For RDMult, a similar phase shift is applied from subcarrier to subcarrier. The beampattern observed in simulations for RDMult is approximately uniform for reasonable values of N_c and the Tx antenna spacing.

C. Computational Complexity

An important practical aspect is the computational complexity required for implementing RDMult. Compared to a traditional SISO OFDM radar, RDMult requires adding a phase shift from subcarrier to subcarrier. This can easily be implemented in the so-called *mapper*, which converts the transmit binary data into symbols, e.g., QPSK symbols. The computational overhead depends on the concrete implementation of the mapper, but it can be considered to be minimal. This is especially true for the choice of $\Delta\varphi_k = \{0, \frac{\pi}{2}, \pi, \frac{3\pi}{2}\}$. For QPSK subcarrier symbols, this phase shift can be implemented by rotating the subcarrier symbols, without changing the QPSK symbol constellation. A similar argumentation holds for higher-order symbol constellations such as 16-QAM.

D. Comparison to ESI

ESI is the currently most prominent multiplexing technique for MIMO OFDM radar systems. An important aspect of ESI is a reduction of the maximum unambiguous range r_max by a factor of N_Tx (when compared to a SISO OFDM system) due to the reduced number of active subcarriers per Tx antenna. The same reduction of r_max is observed for RDMult due to the separation of the range axis into N_Tx areas, cf. Fig. 2.

Processing gain: A significant difference between these multiplexing techniques is given for the processing gain. Since for RDMult, all subcarriers are active at each Tx antenna in every OFDM symbol, it features a processing gain of $G_\text{p} = N_\text{sym}N_\text{c}$. This corresponds to the same processing gain as for SISO OFDM radar systems. In contrast to that, the processing gain for ESI is given by $G_\text{p} = N_\text{sym}N_\text{c}/N_\text{Tx}$ and thus, it is lower than for RDMult.

Average power per active subcarrier: For the sake of a fair comparison, it is assumed that the average transmit power is the same for ESI and RDMult. However, the average power per active subcarrier is not the same due to the different number of active subcarriers. This is indicated in Fig. 5, where exemplary power values of the subcarriers for RDMult and ESI are plotted for the case of $N_\text{Tx} = 4$ and for QPSK symbols. Although the average transmit power is the same for both multiplexing techniques, the average power per active subcarrier for ESI is $N_\text{Tx} = 4$ times larger than for RDMult.

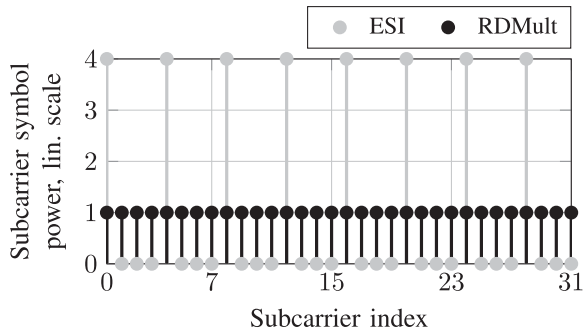

Fig. 5. Exemplary power values of the subcarrier symbols plotted over the subcarrier index for RDMult and for ESI for the case of $N_{\mathrm{Tx}} = 4$ and QPSK symbols. The underlying time-domain signals for RDMult and ESI have the same average power.

SNR in the RDM: First, the situation for ESI is analyzed. There, only the active subcarriers play a role for deriving the RDM for a specific Tx/Rx antenna combination. All other subcarriers are not considered for the evaluation of this RDM. This leads to the following situation. On the one hand, the average power per active subcarrier for ESI is increased by a factor of N_{Tx}. On the other hand, ESI has a decreased processing gain by a factor of N_{Tx} compared to RDMult. Both effects cancel each other out, such that for the same average transmit power, ESI and RDMult attain approximately the same SNR in the RDM. As a further consequence, also the SNR at the output of the DBF is approximately the same for both multiplexing techniques.

Degradation due to ICI: The ICI due to a potential relative velocity of the objects causes a degradation of the SNR [13]. Simulations not shown in this work, as well as the analysis done in [22], show that the SNR degradation due to ICI for RDMult is the same as for ESI.

Computational Complexity: For ESI, the subcarriers are equidistantly allocated to the Tx antennas such that a subcarrier is transmitted on a single Tx antenna only. This allocation is done in the transmitter and can be carried out without additional computational complexity. This is a small advantage of ESI over RDMult, whose computational complexity in the transmitter depends on the choice of $\Delta\varphi_k$ (cf. Section IV-C).

For ESI, the signal processing steps in the radar receiver contain the standard element-wise division with the transmit subcarrier symbols in frequency domain, the range IDFT, and the Doppler DFT. The range IDFT requires $N_{\mathrm{sym}} N_{\mathrm{Tx}}$ IDFT operations of length $N_{\mathrm{c}}/N_{\mathrm{Tx}}$ (in case N_{c} is an integer multiple of N_{Tx}). The Doppler DFT performs $N_{\mathrm{c}}/N_{\mathrm{Tx}}$ DFTs operations of length N_{sym}. These numbers are different for RDMult, which uses N_{sym} IDFT operations of length N_{c} and N_{c} DFT operations of length N_{sym} for range and Doppler processing, respectively. Transferring these DFT/IDFT operations into required numbers of multiplications indicates that the computational complexity in the radar receiver is in general smaller for ESI than for RDMult. The exact amount of multiplications, of course, depends on the parametrization.

V. Communication System Based on RDMult

The specific signal design of RDMult impacts the communication task as well, and is per se not optimal for this purpose, as will be shown. However, a communication system capable of dealing with this specific signal design is proposed in this section. This communication system includes methods for channel estimation, data estimation, and synchronization [27], [30], [31]. Here, the terms 'receiver' and 'Rx antenna' refer to the communication receiver and not to the radar receiver.

TABLE I
Communication System Parameters

Parameter	Value
Bandwidth B	1 GHz
Carrier frequency f_{c}	77 GHz
ADC sampling time T_{s}	1 ns
Number of subcarriers N_{c}	4096
Number of OFDM symbols N_{sym}	512
Length of the cyclic prefix T_{cp}	1 µs
Number of Tx antennas for RDMult and ESI N_{Tx}	4
Number of Rx antennas for RDMult and ESI N_{Rx}	1
Phase shift $\Delta\varphi_k$	$\{0, \frac{\pi}{2}, \pi, \frac{3\pi}{2}\}$

The communication system parameters are listed in Table I. We note, that the proposed communication system is optimized for these parameters. For different parameters, a very similar analysis and optimization may be performed since the observed effects will be very similar. Also note, that the number of Rx antennas N_{Rx} in Table I is set to 1. It will be shown that this is sufficient to enable communication. We note that the signalling framework can easily be extended to the case of multiple receive antennas if required. We would like to emphasize, that $N_{\mathrm{Rx}} = 1$ refers to the communication receiver. The radar receiver itself can have more receive antennas. Hence, in this section, we continue to use the term MIMO OFDM system, or MIMO OFDM joint radar and communication system.

The first part of this section focuses on the channel model for the SISO and MIMO case, followed by establishing an 'effective' channel. It will turn out that it is sufficient to estimate this effective channel rather than the single channels for all possible Tx/Rx combinations. The second part focuses on a channel estimation technique based on preamble OFDM symbols suited for estimating the effective channel. The third part is dedicated to data estimation.

A. Channel Model

Fig. 6 shows the basic transmitter signal processing chain for RDMult as well as the first two receiver signal processing steps. At the transmitter, matrix $\mathbf{S}$ containing the subcarrier symbols is multiplied with $\mathbf{D}^{*}_{N_{\mathrm{c}}}(\frac{\Delta\varphi_k}{2\pi})$ for every antenna index k. The results are then transformed into time domain and extended with the CP. After a convolution of the transmit signal with the N_{Tx} individual channel impulse responses (CIRs), the receiver removes the CP and performs a DFT to recover the received OFDM symbols in frequency domain.

There are three different possibilities in RDMult of representing the communication channel indicated in Fig. 6. The first way is using the CIRs describing the time domain channel from the Tx antennas to the Rx antenna. The second way is using the channel frequency responses (CFRs), which include the CIRs as

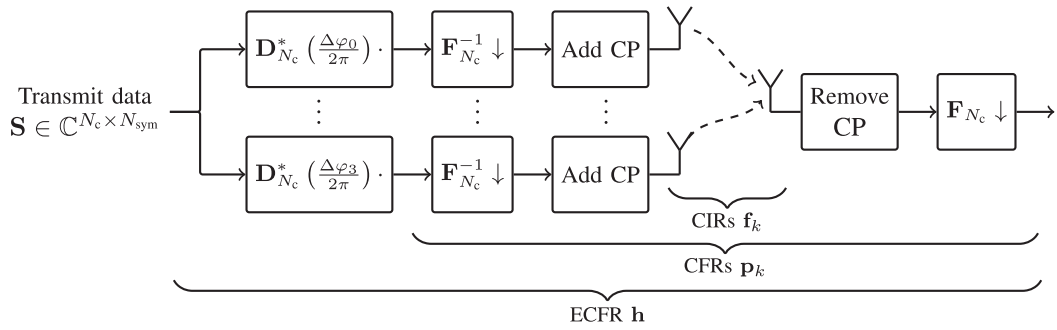

Fig. 6. Visualization of the CIRs, the CFRs, and the ECFR including the signal manipulations. The ADC, analog front-end and the parallel-to-serial conversion are not shown.

well as all processing steps from the IDFTs in the transmitter up to the DFT in the receiver. The third way takes into account that the signals radiated by the different Tx antennas are all based on a single data matrix $\mathbf{S}$. In that case, the CIRs and all shown processing steps form together one SISO channel denoted as effective channel frequency response (ECFR).

Next, the model for the CIRs as well as the representations in form of the CFRs and the ECFR are introduced, followed by a discussion on the ECFR and its implications on the communication system.

1) CIR Representation: The model for generating the CIRs in this work is described in [32], [33]. This model was especially developed for ultrawideband signals and for urban scenarios. The characteristic multipath propagation of urban scenarios in combination with the ultrawideband signals result in sparse impulse responses, where different propagation paths produce narrow bursts in the CIR. These bursts tend to appear in clusters. Code for automated generation of CIRs is available in [34].

Within this code, we have chosen the following parameters: An urban microcell operating scenario, a minimum and maximum Tx-Rx separation of 30 m and 100 m, respectively, 12 dBm transmit power, a base station height of 15 m, 1013.25 mbar pressure, 50 % air humidity, 20° C temperature, no rain, 'Co-Pol' polarization, no foliage loss, and high 'O2I' losses. On the transmit side, we used a uniform linear array (ULA) with $N_\mathrm{Tx} = 4$ elements spaced 2 times the wavelength apart. The 3 dB half-power bandwidth (HPBW) of all antennas was chosen to be 20 degrees.

The discrete-time representation of a CIR is denoted in vector form as $\mathbf{f} \in \mathbb{C}^{N_\mathbf{f}}$. For the chosen sampling time T_s in Table I, a statistical evaluation based on a large set of generated CIRs confirms an assumed CIR length of $N_\mathbf{f} = 256$ to be sufficient for adequate modelling.

For the MIMO case, the N_Tx individual CIRs are denoted as $\mathbf{f}_k \in \mathbb{C}^{N_\mathbf{f}}$, $0 \leq k < N_\mathrm{Tx}$. Since the antenna spacing is usually much smaller than the propagation distance between transmitter and receiver, the individual CIRs will be correlated. The effect is known as spatial correlation [33], [35], [36] and is accounted for by the code provided in [34].

2) CFR Representation: The CFRs are obtained via

$$\mathbf{p}_k = \mathbf{F}_{N_\mathrm{c}} \mathbf{B}_\mathrm{zp} \mathbf{f}_k \in \mathbb{C}^{N_\mathrm{c}}. \tag{15}$$

TABLE II
SCHEMATIC VISUALIZATION OF THE FIRST 5 ELEMENTS OF $\mathbf{b}_k$, $0 \leq K < 4$ AND $\mathbf{h}$ FOR AWGN CHANNELS. THE ARROWS INDICATE THE MAGNITUDE AND PHASE OF A COMPLEX-VALUED SCALAR IN THE COMPLEX PLANE

	$\mathbf{b}_0$	$\mathbf{b}_1$	$\mathbf{b}_2$	$\mathbf{b}_3$	$\mathbf{h}$
$m=0$	$\rightarrow$	$\rightarrow$	$\rightarrow$	$\rightarrow$	$\longrightarrow$
$m=1$	$\rightarrow$	$\downarrow$	$\leftarrow$	$\uparrow$	zero
$m=2$	$\rightarrow$	$\leftarrow$	$\rightarrow$	$\leftarrow$	zero
$m=3$	$\rightarrow$	$\uparrow$	$\leftarrow$	$\downarrow$	zero
$m=4$	$\rightarrow$	$\rightarrow$	$\rightarrow$	$\rightarrow$	$\longrightarrow$

The matrix $\mathbf{B}_\mathrm{zp} \in \mathbb{C}^{N_\mathrm{c} \times N_\mathbf{f}}$ zero-pads the CIRs $\mathbf{f}_k$ of length $N_\mathbf{f} = 256$ to a length of $N_\mathrm{c} = 4096$. $\mathbf{F}_{N_\mathrm{c}}$ transforms the zero-padded CIRs into the frequency domain. Hence, each element of $\mathbf{p}_k$ corresponds to a subcarrier.

3) ECFR Representation: The ECFR is denoted as $\mathbf{h} \in \mathbb{C}^{N_\mathrm{c}}$ and, according to Fig. 6, can be derived as

$$\mathbf{h} = \sum_{k=0}^{N_\mathrm{Tx}-1} \mathbf{b}_k, \tag{16}$$

where $\mathbf{b}_k \in \mathbb{C}^{N_\mathrm{c}}$ is given as

$$\mathbf{b}_k = \mathbf{D}^*_{N_\mathrm{c}}\left(\frac{\Delta\varphi_k}{2\pi}\right)\mathbf{p}_k. \tag{17}$$

4) Properties of the ECFR: Equation (16) shows that the ECFR is given by the sum of N_Tx terms. These terms may add up constructively or destructively. It turns out that the constructive/destructive interference appears in a special pattern along the subcarriers. This pattern is caused by the matrices $\mathbf{D}^*_{N_\mathrm{c}}(\frac{\Delta\varphi_k}{2\pi})$, and it can be nicely shown for the case of additive white Gaussian noise (AWGN) channels, since for this case (17) reduces to $\mathbf{b}_k = \mathbf{D}^*_{N_\mathrm{c}}(\frac{\Delta\varphi_k}{2\pi})\mathbf{1}^{N_\mathrm{c}}$. These terms $\mathbf{b}_k$ for $0 \leq k < N_\mathrm{Tx}$ are sketched in form of arrows for the first 5 subcarriers $0 \leq m < 5$ in Table II. For the choice of $\Delta\varphi_k = \{0, \frac{\pi}{2}, \pi, \frac{3\pi}{2}\}$, the elements of $\mathbf{b}_0$ are not affected by any phase shift. The elements of $\mathbf{b}_1$ are affected by a phase shift of $-\frac{\pi}{2}$ from subcarrier to subcarrier, and so on. Table II also sketches the first 5 elements of the ECFR $\mathbf{h}$. This ECFR is evaluated via (16) and it reveals that the ECFR at the subcarriers $m = 0,\ 4,\ 8, \ldots$ will observe constructive interference, while the ECFR at all other subcarriers

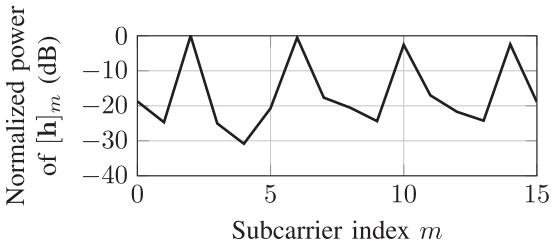

Fig. 7. Normalized power of an exemplary ECFR plotted over the subcarrier index m.

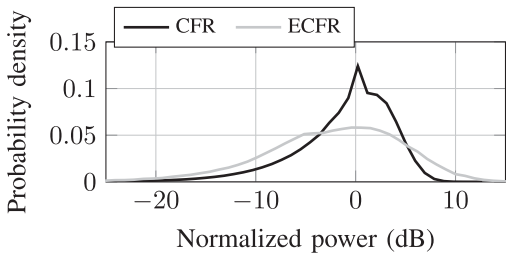

Fig. 8. Estimated distribution of the magnitude values of the CFR and ECFR channel coefficients.

will be zero. Thus, a pattern with length 4 is observed. The length of this pattern is due to the choice of $\Delta\varphi_k$.

In case of a frequency selective channel, e.g., as described earlier in this section, this effect will not be that severe as for the AWGN case in Table II. Nevertheless, constructive/destructive interference is still an issue. This is demonstrated in Fig. 7, which shows the normalized power of the first 16 subcarriers of an exemplary ECFR. A repetitive pattern with a length of 4 subcarriers is clearly visible. It is worth noting the difference in power between the strong subcarriers (e.g. at $m = 2$) and the weak subcarriers (e.g. at $m = 4$). This huge difference is typical for the ECFR and can be explained the following way. The ECFR is given by the sum of N_{Tx} terms according to (16). These terms contain the N_{Tx} individual CFRs $\mathbf{p}_k$ according to (17). The individual CFRs are correlated due to the mentioned effect of spatial correlation, which causes similar magnitude values for a subcarrier in all N_{Tx} CFRs. Due to these similar magnitude values, and due to the rotating phase values caused by the phase shift $\Delta\varphi_k$, destructive interference produces so-called deep fading holes in the ECFR. These deep fading holes can be observed as weak subcarriers in Fig. 7, which explains the difference in power between the strong and weak subcarriers.

A statistical analysis of this effect is presented in Fig. 8 showing averaged histograms as estimates of the probability density functions (PDFs) of the magnitude values of the CFR and ECFR channel coefficients. These histograms were evaluated over 1000 channel realizations, where every channel was normalized to 0 dB average power. These estimated PDFs clearly show that deep fading holes are more likely for the ECFR than for the CFRs.

A consequence of these deep fading holes is that several subcarriers will be less qualified for transmission. Hence, methods for robustifying the communications are required.

5) Increasing Robustness of the Communications: A common means for increasing the robustness is incorporating redundancy, e.g., by applying an adequate channel code, which compensates for the non-idealities of the communication channel. Experiments not detailed in this work demonstrated that applying a well-known [30] and usually powerful enough convolutional code with code rate $r = 1/2$ was not strong enough to cope with the distortions coming along with the considered channels. More specifically, the repetitive attenuation pattern and the thereof resulting large number of fading holes overstrained the possibilities of the applied code. A natural consequence would be the utilization of a channel code with a lower coding rate. However, the inherently increased computational complexity of the channel decoder in combination with the real-time constraints of the considered application limit the applicability of this alternative. Furthermore, taking into account the information about the attenuation pattern might be rather difficult.

In this work, we propose to use a well-known convolutional channel code with rate $r = 1/2$, but additionally add further redundancy by transmitting the same data on 4 subcarriers in parallel. These sets of subcarriers shall be selected taking into account the observed attenuation pattern sketched in Fig. 7. As such, the knowledge about the pattern can be utilized and explicitly incorporated in the design while ensuring a moderate computational complexity in the decoding process. This approach is inspired by space-frequency codes [37], [38], [39]. Similar to these codes, our approach uses diversity gain to increase the robustness of the communications. Adding redundancy naturally entails a reduction in data rate. Fortunately, this data rate reduction may be considered a rather moderate disadvantage for OFDM-based systems, since the large bandwidths usually employed for radar sensing applications allow for extraordinary high data rates, which by far exceed those of competitive radar waveforms [40].

Transmitting the same data on 4 subcarriers in parallel is formally described by constructing the data matrix $\mathbf{S}$ in (6) according to

$$\mathbf{S} = \mathbf{B}\mathbf{X} \tag{18}$$

where $\mathbf{B} \in \mathbb{R}^{N_{\mathrm{c}} \times N_{\mathrm{c}}/4}$ is given by

$$\mathbf{B} = \begin{bmatrix} \mathbf{M} & \mathbf{0} & \dots & \mathbf{0} \\ \mathbf{0} & \mathbf{M} & & \vdots \\ \vdots & & \ddots & \mathbf{0} \\ \mathbf{0} & \dots & \mathbf{0} & \mathbf{M} \end{bmatrix}, \tag{19}$$

with the matrix $\mathbf{M}$ defined as

$$\mathbf{M} = \begin{bmatrix} 1 & 0 & 0 & 0 & 0 & 0 & 1 & 0 & 0 & 1 & 0 & 0 & 0 & 0 & 0 & 1 \\ 0 & 0 & 1 & 0 & 1 & 0 & 0 & 0 & 0 & 0 & 0 & 1 & 0 & 1 & 0 & 0 \\ 0 & 1 & 0 & 0 & 0 & 0 & 0 & 1 & 0 & 0 & 1 & 0 & 1 & 0 & 0 & 0 \\ 0 & 0 & 0 & 1 & 0 & 1 & 0 & 0 & 1 & 0 & 0 & 0 & 0 & 0 & 1 & 0 \end{bmatrix}^T \in \mathbb{R}^{16 \times 4}. \tag{20}$$

The matrix $\mathbf{M}$ is designed such that a subcarrier symbol within $\mathbf{X} \in \mathbb{C}^{N_{\mathrm{c}}/4 \times N_{\mathrm{sym}}}$ is spread over 4 non-neighboring subcarriers

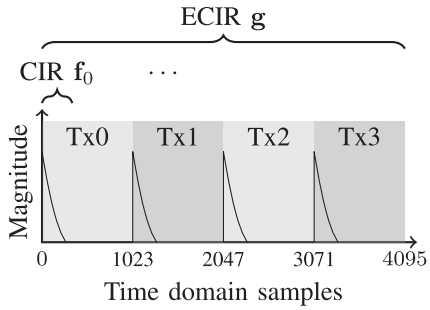

Fig. 9. Schematic visualization of the relation between the CIRs and the ECIR.

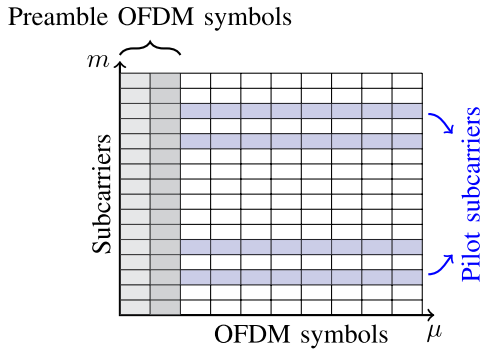

Fig. 10. Exemplary allocation of preamble OFDM symbols and pilot subcarriers.

and such that a distance of 4 between the redundant subcarrier symbols is avoided.

6) Properties of the ECIR: The counterpart of the ECFR $\mathbf{h}$ in time domain is the effective channel impulse response (ECIR) $\mathbf{g} \in \mathbb{C}^{N_\mathrm{c}}$ obtained by applying an IDFT on $\mathbf{h}$ according to

$$\mathbf{g} = \mathbf{F}_{N_\mathrm{c}}^{-1}\mathbf{h} = \sum_{k=0}^{N_\mathrm{Tx}-1} \mathbf{F}_{N_\mathrm{c}}^{-1}\mathbf{D}_{N_\mathrm{c}}^{*}\left(\frac{\Delta\varphi_k}{2\pi}\right)\mathbf{F}_{N_\mathrm{c}}\mathbf{B}_\mathrm{zp}\mathbf{f}_k. \tag{21}$$

According to (21), the ECIR consists of N_Tx components $0 \leq k < N_\mathrm{Tx}$. For every component, the phase shift $\Delta\varphi_k$ from subcarrier to subcarrier in the frequency domain corresponds to a circular shift of the zero-padded CIRs $\mathbf{B}_\mathrm{zp}\mathbf{f}_k$ in time domain by $N_\mathrm{c}\frac{\Delta\varphi_k}{2\pi}$ samples. For the choices of $\Delta\varphi_k = \{0, \frac{\pi}{2}, \pi, \frac{3\pi}{2}\}$ and $N_\mathrm{c} = 4096$, the first component at $k = 0$ is not shifted, the second at $k = 1$ is shifted by 1024 samples, the third at $k = 2$ by 2048 samples, and the fourth component at $k = 3$ by 3072 samples. All four components as well as the resulting ECIR are sketched in Fig. 9. There, $N_\mathrm{Tx} = 4$ areas are marked, each one corresponding to a specific Tx antenna, with the corresponding CIR $\mathbf{f}_k$, $0 \leq k < N_\mathrm{Tx}$ of length $N_\mathbf{f} = 256$ at the beginning, followed by zero padding up to 1024 samples in total per area. The knowledge of zero padding will later be exploited for enhancing the accuracy of the channel estimate.

B. Signal Model

In the following, a model for the receive signal of the communication receiver is introduced. This signal model is related to (4) for the radar receiver, but it employs the channel model discussed in Section V-A. With $\mathbf{H} = \mathrm{diag}(\mathbf{h})\mathbf{B} \in \mathbb{C}^{N_\mathrm{c}\times N_\mathrm{c}/4}$, and (18), the received time domain OFDM symbols after removing the CP are given by

$$\mathbf{Y}_\mathrm{tf,ts} = \mathbf{F}_{N_\mathrm{c}}^{-1}\mathrm{diag}\left(\mathbf{h}\right)\mathbf{S}\mathbf{\Lambda} + \mathbf{N} \in \mathbb{C}^{N_\mathrm{c}\times N_\mathrm{sym}} \tag{22}$$

$$= \mathbf{F}_{N_\mathrm{c}}^{-1}\mathbf{H}\mathbf{X}\mathbf{\Lambda} + \mathbf{N}, \tag{23}$$

where $\mathbf{N} \in \mathbb{C}^{N_\mathrm{c}\times N_\mathrm{sym}}$ contains uncorrelated zero-mean white Gaussian noise samples with variance σ_n^2. The elements of the diagonal matrix $\mathbf{\Lambda} \in \mathbb{C}^{N_\mathrm{sym}\times N_\mathrm{sym}}$ model the CPE and are given by $\mathrm{e}^{j\varphi_\mu}$ with φ_μ representing the unknown CPE for the μth OFDM symbol.

Let the μth column of $\mathbf{Y}_\mathrm{tf,ts}$ be denoted as $\mathbf{y}_\mu \in \mathbb{C}^{N_\mathrm{c}}$. The corresponding frequency domain OFDM symbol is obtained by applying a DFT on $\mathbf{y}_\mu$

$$\mathbf{z}_\mu = \mathbf{F}_{N_\mathrm{c}}\mathbf{y}_\mu \in \mathbb{C}^{N_\mathrm{c}}. \tag{24}$$

The μth column of $\mathbf{X}$ is denoted as $\mathbf{x}_\mu \in \mathbb{C}^{N_\mathrm{c}/4}$ such that $\mathbf{x}_\mu$ and $\mathbf{z}_\mu$ are connected via

$$\mathbf{z}_\mu = \mathrm{diag}\left(\mathbf{h}\right)\mathbf{s}_\mu\mathrm{e}^{\mathrm{j}\varphi_\mu} + \mathbf{n}_\mu \tag{25}$$

$$= \mathbf{H}\mathbf{x}_\mu\mathrm{e}^{\mathrm{j}\varphi_\mu} + \mathbf{n}_\mu, \tag{26}$$

whereas $\mathbf{n}_\mu \in \mathbb{C}^{N_\mathrm{c}}$ is the DFT transform of the μth column of $\mathbf{N}$. The vector $\mathbf{x}_\mu$ contains data symbols as well as pilot symbols used for synchronization later in this work. The number of pilot symbols is denoted as N_p, while the number of data symbols is denoted as N_d with $N_\mathrm{c}/4 = N_\mathrm{p} + N_\mathrm{d}$

C. Channel Estimation

The following investigations focus on methods for estimating the ECFR. A common means for channel estimation is the utilization of preamble OFDM symbols known to the receiver [30], [41]. Fig. 10 shows the allocation of $N_\mathrm{pr} = 2$ preamble OFDM symbols, however, a modification to more or less preamble OFDM symbols is straightforward. The received preamble OFDM symbols are potentially affected by an unknown CPE due to a possible relative velocity between transmitter and receiver [42], [43]. This unknown CPE must be accounted for by the channel estimation method.

The first N_pr columns of $\mathbf{X}$ contain the preamble symbols. For the sake of simplicity, it is assumed that the same preamble symbols denoted as $\mathbf{x}_\mathrm{pr} \in \mathbb{C}^{N_\mathrm{c}/4}$ are transmitted N_pr times such that $\mathbf{x}_\mu = \mathbf{x}_\mathrm{pr}$ for $0 \leq \mu < N_\mathrm{pr}$. With (18), the preamble OFDM symbol can be derived as $\mathbf{s}_\mathrm{pr} = \mathbf{B}\mathbf{x}_\mathrm{pr}$.

Equation (25) serves as a basis for channel estimation. Exchanging the roles of the channel and the transmit symbols, and incorporating (21), yields

$$\mathbf{z}_\mu = \mathbf{S}_\mathrm{pr}\mathbf{F}_{N_\mathrm{c}}\mathbf{g}\mathrm{e}^{\mathrm{j}\varphi_\mu} + \mathbf{n}_\mu, \tag{27}$$

where $\mathbf{S}_\mathrm{pr} = \mathrm{diag}(\mathbf{s}_\mathrm{pr})$. Without loss of generality, we assume $\varphi_0 = 0$ and estimate the CPE of the μth received preamble OFDM symbol with respect to (w.r.t.) the first preamble OFDM symbol via [31], [44], [45]

$$\widehat{\varphi}_\mu = \arg\left(\mathbf{z}_0^H\mathbf{z}_\mu\right), \tag{28}$$

with $\widehat{\cdot}$ indicating an estimate. This estimated CPE is used for synchronizing the received preamble OFDM symbols according to

$$\widetilde{\mathbf{z}}_\mu = \mathbf{z}_\mu \cdot \mathrm{e}^{-\mathrm{j}\widehat{\varphi}_\mu}. \tag{29}$$

After performing this synchronization step for $0 \leq \mu < N_{\mathrm{pr}}$, the synchronized preamble OFDM symbols are averaged according to [41]

$$\bar{\widetilde{\mathbf{z}}} = \frac{1}{N_{\mathrm{pr}}} \sum_{\mu=0}^{N_{\mathrm{pr}}-1} \widetilde{\mathbf{z}}_\mu. \tag{30}$$

By utilizing $\bar{\widetilde{\mathbf{z}}}$, the model in (27) reduces to

$$\bar{\widetilde{\mathbf{z}}} \approx \mathbf{S}_{\mathrm{pr}} \mathbf{F}_{N_{\mathrm{c}}} \mathbf{g} + \bar{\mathbf{n}}, \tag{31}$$

whereas

$$\bar{\mathbf{n}} = \frac{1}{N_{\mathrm{pr}}} \sum_{\mu=0}^{N_{\mathrm{pr}}-1} \mathbf{n}_\mu. \tag{32}$$

Based on (31), one can use the commonly employed best linear unbiased estimator (BLUE) for ECIR estimation [30], [41], [46], [47]. Since $\mathbf{S}_{\mathrm{pr}}\mathbf{F}_{N_{\mathrm{c}}}$ in (31) is invertible, the BLUE for the ECIR reduces to [46]

$$\widehat{\mathbf{g}} = \mathbf{M}_{\mathrm{z}}^T \mathbf{M}_{\mathrm{z}} \mathbf{F}_{N_{\mathrm{c}}}^{-1} \mathbf{S}_{\mathrm{pr}}^{-1} \bar{\widetilde{\mathbf{z}}} \in \mathbb{C}^{N_{\mathrm{c}}}, \tag{33}$$

where $\mathbf{M}_{\mathrm{z}} \in \mathbb{C}^{N_{\mathbf{f}} N_{\mathrm{Tx}} \times N_{\mathrm{c}}}$ is a selection matrix that dismisses the areas within the ECIR containing zeros only (cf. Section V-A6). The BLUE for the ECFR follows as

$$\widehat{\mathbf{h}} = \mathbf{F}_{N_{\mathrm{c}}} \widehat{\mathbf{g}} \in \mathbb{C}^{N_{\mathrm{c}}}. \tag{34}$$

Finally, an estimate for $\mathbf{H}$ is obtained via

$$\widehat{\mathbf{H}} = \mathrm{diag}\left(\widehat{\mathrm{h}}\right) \mathbf{B} \in \mathbb{C}^{N_{\mathrm{c}} \times N_{\mathrm{c}}/4}. \tag{35}$$

D. Data Estimation

A CPE due to a relative velocity has to be considered for data estimation as well, which is known as synchronization. Synchronization is achieved using pilot subcarriers indicated in Fig. 10.

Replacing $\mathbf{H}$ in (26) by its estimate $\widehat{\mathbf{H}}$ from (35), and introducing $\mathbf{w}_\mu = \mathbf{x}_\mu \mathrm{e}^{\mathrm{j}\varphi_\mu} \in \mathbb{C}^{N_{\mathrm{c}}/4}$ allows rewriting (26) as

$$\mathbf{z}_\mu \approx \widehat{\mathbf{H}} \mathbf{w}_\mu + \mathbf{n}_\mu. \tag{36}$$

This result allows applying the linear minimum mean square error (LMMSE) estimator for estimating $\mathbf{w}_\mu$ as [31], [46], [48]

$$\widehat{\mathbf{w}}_\mu = \left(\widehat{\mathbf{H}}^H \widehat{\mathbf{H}} + N_{\mathrm{c}} \sigma_n^2 \mathbf{C}_{\mathbf{xx}}^{-1}\right)^{-1} \widehat{\mathbf{H}}^H \mathbf{z}_\mu, \tag{37}$$

where $\mathbf{C}_{\mathbf{xx}} \in \mathbb{C}^{N_{\mathrm{c}} \times N_{\mathrm{c}}}$ is the covariance matrix of $\mathbf{x}_\mu$. For the sake of brevity, $\mathbf{C}_{\mathbf{xx}}$ is assumed to be a diagonal matrix whose elements are given by the average power (averaged over μ) of the subcarrier symbols within $\mathbf{x}_\mu$. The error covariance matrix of the estimates in (37) is given by [31], [46], [47]

$$\mathbf{C}_{\mathbf{ee}} = N_{\mathrm{c}} \sigma_n^2 \left(\widehat{\mathbf{H}}^H \widehat{\mathbf{H}} + N_{\mathrm{c}} \sigma_n^2 \mathbf{C}_{\mathbf{xx}}^{-1}\right)^{-1}. \tag{38}$$

The vector $\widehat{\mathbf{w}}_\mu$ in (37) is a CPE distorted estimate of $\mathbf{x}_\mu$. Thus, $\widehat{\mathbf{w}}_\mu$ contains CPE distorted estimates of data symbols and pilot symbols. The sub-vector containing the estimated data symbols only is denoted as $\widehat{\mathbf{w}}_\mu^{\mathrm{d}} \in \mathbb{C}^{N_{\mathrm{d}}}$, and the sub-vector containing the estimated pilot symbols only is denoted as $\widehat{\mathbf{w}}_\mu^{\mathrm{p}} \in \mathbb{C}^{N_{\mathrm{p}}}$. The CPE is estimated through [31], [44], [45]

$$\widehat{\varphi}_\mu = \arg\left(\left(\mathbf{x}_\mu^{\mathrm{p}}\right)^H \mathbf{W}\, \widehat{\mathbf{w}}_\mu^{\mathrm{p}}\right), \tag{39}$$

where $\mathbf{x}_\mu^{\mathrm{p}} \in \mathbb{C}^{N_{\mathrm{p}}}$ is a vector containing the known true pilot symbols, and where $\mathbf{W} \in \mathbb{C}^{N_{\mathrm{p}} \times N_{\mathrm{p}}}$ is an optional diagonal weighting matrix to rate the pilots regarding their estimation quality. This weighting matrix $\mathbf{W}$ might be constructed based on the inverse main diagonal elements of the error covariance matrix $\mathbf{C}_{\mathbf{ee}}$ in (38). Finally, the CPE is compensated via

$$\widehat{\widetilde{\mathbf{x}}}_\mu^{\mathrm{d}} = \widehat{\mathbf{w}}_\mu^{\mathrm{d}} \cdot \mathrm{e}^{-\mathrm{j}\widehat{\varphi}_\mu} \in \mathbb{C}^{N_{\mathrm{d}}}, \tag{40}$$

which represents the desired estimated data symbols.

VI. Simulation Setup and Performance Comparison

In this section, the BER performance of the proposed MIMO OFDM system using RDMult is investigated. This BER performance is compared with that of a SISO OFDM system [27], [30], [31], with that of a MIMO OFDM system using ESI, and with that of a MIMO OFDM system using the non-equidistant dynamic subcarrier interleaving (NeqDySI) technique proposed in [26]. For the latter one, we assume that the receiver perfectly knows the allocation of the Tx antennas to the subcarriers from the transmitter.

The system parameters of the MIMO OFDM systems are listed in Table I. The SISO OFDM system employs the same parameters except for $N_{\mathrm{Tx}} = 1$. Since only the MIMO OFDM system using RDMult has to deal with the constructive/destructive interference pattern visualized in Fig. 7, it is the only system that adds additional redundancy by means of (18).

The transmitters of all four systems employ a convolutional channel code with coding rate $r = 1/2$, constraint length 7 and the generator polynomials $(133, 171)_8$ in octal representation [30], [31].[2] The encoded bits are interleaved by a random interleaver with a block length equal to the number of coded bits in an OFDM symbol. The mapper transforms the binary data into QPSK symbols. On the receiver side, the demapper extracts the log-likelihood ratios (LLRs) from the estimated data symbols [50], [51], [52], followed by a deinterleaver and a Viterbi decoder with soft decision decoding. The time domain noise variance σ_{n}^2 is set to obtain a desired E_{b}/N_0 value measured at the receiver input. There, E_{b} denotes the average energy per bit of information, and $N_0/2$ denotes the double-sided noise power spectral density of a bandpass noise signal [31]. Thus, E_{b}/N_0 serves as a measure for the SNR. The variance σ_{n}^2 is given by [53]

$$\sigma_{\mathrm{n}}^2 = \frac{P_{\mathrm{s}}}{(E_{\mathrm{b}}/N_0) r b \zeta \nu}, \tag{41}$$

[2]The same code has been used during the standardization process of the IEEE802.11a standard [49].

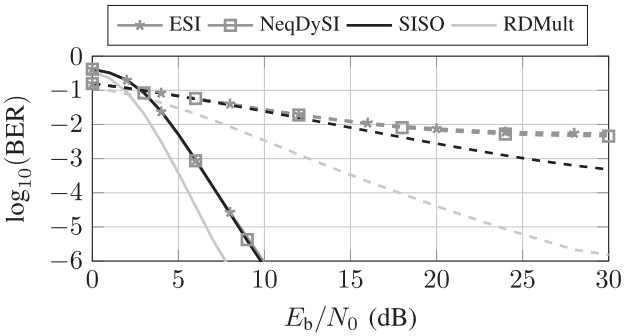

Fig. 11. BER curves for coded (solid) and uncoded (dashed) transmission with perfect channel knowledge and perfect synchronization. The curves for SISO, ESI and NeqDySI in the coded case lie on top of each other.

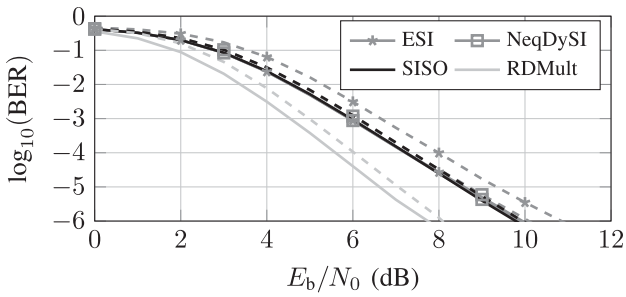

Fig. 12. BER curves for coded ($r = 1/2$) transmission with perfect synchronization. The solid lines are with perfect channel knowledge, and the dashed lines are with imperfect channel estimation based on preamble OFDM symbols. The curves for SISO and ESI with perfect channel knowledge lie on top of each other.

where P_s represents the average power per time domain sample measured at the receiver input. The parameter ζ is defined as $\zeta = N_c/(N_{cp} + N_c)$ and accounts for the samples in the CP. b corresponds to the number of coded bits per data symbol and is set to 2 due to the considered QPSK symbol alphabet. The redundancy by means of (18) is accounted for by ν. Hence, ν is set to $\frac{1}{4}$ for the MIMO OFDM system with RDMult, while it is set to 1 for all other systems. Thus, the MIMO OFDM system with RDMult will observe a higher noise variance σ_n^2 compared to the competitive systems.

For zero relative velocity, the channels are quasi-static, meaning that they stay constant during the transmission of one burst of N_{sym} OFDM symbols and then change to independent channel realizations for the next burst. For the considered case of non-zero relative velocity, whose effects are accounted for via an ICI and a CPE, the channels are not quasi-static anymore. This relative velocity is randomly drawn from a uniform distribution between ± 60 m/s for every burst. The BER performances were evaluated by averaging over 10 000 randomly generated channel instances, whereas 5 000 represent line of sight (LOS) and the other 5 000 represent non-line of sight (NLOS) scenarios.

In the following, four simulation scenarios and the resulting BER performances are described.

1) Perfect Channel Knowledge; Perfect CPE Synchronization: Fig. 11 visualizes the resulting BER curves for perfect channel knowledge and perfect synchronization between transmitter and receiver. There, coded and uncoded transmission is considered. In both cases, the MIMO OFDM system with RDMult significantly outperforms the SISO OFDM system as well as the MIMO OFDM systems with ESI and NeqDySI. The increase in performance obtained for the MIMO OFDM system with RDMult is approximately 1.8 dB in the coded case and can be explained by the diversity gain discussed in Section V-A5.

For the sake of completeness, it shall be noted that also the performances of the other communication systems would increase when adding additional redundancy as done for RDMult at the cost of a reduced data rate. In fact, adding the same redundancy also to ESI would lead to a quite similar BER performance as observed for RDMult.

In the remainder of this work, uncoded transmission is not shown anymore due to its minor practical relevance.

2) Perfect CPE Synchronization; Imperfect Channel Estimation Using Preamble OFDM Symbols: The second simulation investigates the impact of imperfect channel knowledge on the BER performance. The channel estimation procedures for a SISO OFDM system and for a MIMO OFDM system using ESI consist of similar steps as discussed in Section V-C. Both derivations are omitted in this work for the sake of brevity.

In order to distinctly carry out the difference of the systems in terms of sensitivity to channel estimation errors, we aim at comparing the performance of them for the same distortion properties. We therefore set $N_{pr} = 2$ for the SISO OFDM system and for the MIMO OFDM system using ESI, and $N_{pr} = 8$ for the MIMO OFDM system using RDMult, which in combination with the different values for σ_n^2 result then in the same effective SNR conditions when averaging over the N_{pr} preambles.

For the MIMO OFDM system using NeqDySI, the channels between all $N_{Tx} = 4$ transmit antennas and the receive antenna are estimated separately with $N_{pr} = 2$ preamble OFDM symbols each. During those in total 8 preamble OFDM symbols only a single Tx antenna occupies all N_c subcarriers. This ensures the same effective SNR per estimated channel as for the other systems.

Fig. 12 visualizes the resulting BER curves as well as the curves for perfect channel knowledge from Fig. 11 as reference. This comparison indicates that the MIMO OFDM systems using ESI and RDMult are more sensitive to imperfect channel information than the SISO OFDM system and the MIMO OFDM system utilizing NeqDySI.

3) Perfect Channel Knowledge; Imperfect CPE Synchronization Using Pilot Subcarriers: The third simulation assumes perfect channel knowledge, while synchronization is performed using pilot subcarriers. The number of pilot subcarriers for the SISO OFDM system and for the MIMO OFDM systems using ESI and NeqDySI is set to 16. Both systems employ a standard pilot-based synchronization procedure similar to that discussed in Section V-D and in [31]. The MIMO OFDM system using RDMult employs 16 pilot symbols within $\mathbf{x}_\mu$, which translates to 64 pilot subcarriers within $\mathbf{s}_\mu$ according to (18). This ensures the same effective SNR as discussed previously.

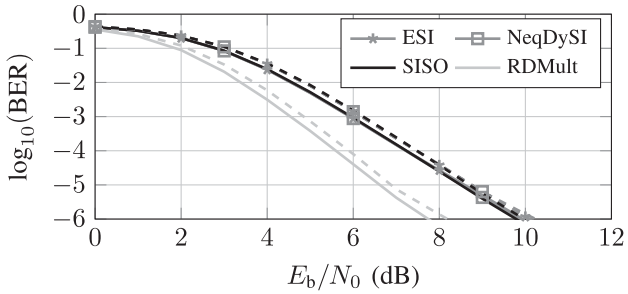

Fig. 13. BER curves for coded ($r = 1/2$) transmission with perfect channel knowledge. The solid lines are with perfect synchronization, and the dashed lines are with imperfect synchronization based on pilot subcarriers. The curves for SISO, ESI, and NeqDySI lie on top of each other.

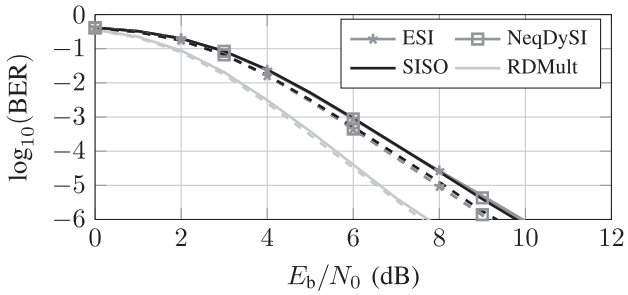

Fig. 14. BER curves for coded transmission with with perfect channel knowledge and perfect synchronization. The simulations were carried out with (solid) and without (dashed) ICI-induced distortions. The curves for SISO, ESI, and NeqDySI lie on top of each other.

The 16 pilot symbols within $\mathbf{x}_\mu$ were allocated equidistantly and their positions were kept constant for all simulations. The first pilot symbol is at index 33 and all other pilot symbols follow with a spacing of 64 indices. A very similar equidistant placement of the subcarriers is employed for all other communication systems.

The resulting BER curves are shown in Fig. 13 together with the BER curves for the case of perfect synchronization. These curves reveal that all systems behave similar to imperfect synchronization with a rather moderate loss in performance.

4) Perfect Channel Knowledge; Perfect CPE Synchronization; Disabled ICI: For the last simulation scenario of this work, the influence of ICI on the BER performance is investigated. This simulation scenario assumes perfect channel knowledge and perfect CPE synchronization. Fig. 14 shows the resulting BER curves with and without ICI-induced distortions. One can observe that the BER degradations due to ICI are slightly smaller for RDMult than for all other considered multiplexing techniques.

VII. Conclusion

In this work, a novel MIMO OFDM joint radar sensing and communication systems especially designed for the use in combination with RDMult was proposed. RDMult modifies the transmitted OFDM signals such that signal components radiated by different Tx antennas can be separated along the range axis in the RDM. A detailed analysis of RDMult for the radar sensing task was carried out, which led to the insight that the SNR performance of RDMult is approximately the same as for ESI. In fact, these analysis confirmed that the RDMult shows approximately the same performance as ESI for the radar sensing task in terms of

- the maximum unambiguous range,
- the SNR in the RDM,
- the SNR at the output of the DBF.

In contrast to that, differences between RDMult and ESI for the radar sensing task were observed for

- the processing gain, and
- the average power per active subcarrier.

The special transmit signals generated by RDMult were analyzed w.r.t. the communication task. We showed that a SISO channel, denoted as 'effective' channel, is sufficient for describing the communication channel, although several Tx antennas are involved. It turned out that this effective channel is affected by constructive/destructive interferences of the underlying CFRs, which may cause a pattern of deep fading holes in the ECFR. This problem was combated by adding additional redundancy in the transmit data especially designed for dealing with the pattern of deep fading holes. This led to a very good BER performance at the cost of a reduced data rate. Based on the ECFR and the additional redundancy, a communication setup including methods for data estimation, channel estimation and synchronization was proposed.

Appendix A.
Range Shift Induced by $\Delta\varphi_k$

In this appendix we prove that an additional phase shift of $\Delta\varphi_k = 2\pi\frac{p}{N_c}$ with $p \in \mathbb{Z}$ results in a circular shift by p range bins without any distortions of the amplitude or phase.

The phase shift $\Delta\varphi_k$ can be found in the argument of $\mathbf{u}^*_{N_c}(\frac{\Delta\varphi_k}{2\pi} + \bar{\tau}_{i,k})$ in (14). To improve the readability, this expression is reformulated to $\mathbf{u}^*_{N_c}(\frac{\Delta\varphi_k}{2\pi} + \tau)$.

At first, the same expression without the phase shift $\Delta\varphi_k$ is inspected as a reference. According to the definition in (12), the tth element of $\mathbf{u}^*_{N_c}(\tau)$ with $0 \le t < N_c$ is given by

$$\left[\mathbf{u}^*_{N_c}(\tau)\right]_t = \sum_{n=0}^{N_c-1} \mathrm{e}^{-\mathrm{j}2\pi\left(\tau-\frac{t}{N_c}\right)n}, \tag{42}$$

where the real-valued window function $w_{N_c}[n]$ has been ignored to further improve the readability. Note that the right-hand side of (42) is periodic in t with a period of N_c. Next, including the phase shift results in

$$\left[\mathbf{u}^*_{N_c}\left(\frac{\Delta\varphi_k}{2\pi}+\tau\right)\right]_t = \sum_{n=0}^{N_c-1} \mathrm{e}^{-\mathrm{j}2\pi\left(\frac{\Delta\varphi_k}{2\pi}+\tau-\frac{t}{N_c}\right)n}, \tag{43}$$

Choosing $\Delta\varphi_k = 2\pi\frac{p}{N_c}$ with $p \in \mathbb{Z}$ allows rewriting (43) according to

$$\left[\mathbf{u}^*_{N_c}\left(\frac{\Delta\varphi_k}{2\pi}+\tau\right)\right]_t = \sum_{n=0}^{N_c-1} \mathrm{e}^{-\mathrm{j}2\pi\left(\tau-\frac{t-p}{N_c}\right)n}. \tag{44}$$

Note that the right-hand side of (44) is periodic in t and p with a period of N_c. Comparing (44) with (42), and considering the mentioned periodicity, shows that the elements of the vector $\mathbf{u}^*_{N_c}(\frac{\Delta\varphi_k}{2\pi}+\tau)$ are circularly shifted by p elements compared to the elements of the vector $\mathbf{u}^*_{N_c}(\tau)$. Since these elements correspond to the range bins of the RDM, one can state that peaks in the RDM are shifted by p range bins. The comparison of (44) with (42) also shows that this shift is achieved without any distortions of the magnitude or phase values.

REFERENCES

[1] S. Sun, A. P. Petropulu, and H. V. Poor, "MIMO radar for advanced driver-assistance systems and autonomous driving: Advantages and challenges," *IEEE Signal Process. Mag.*, vol. 37, no. 4, pp. 98–117, Jul. 2020.

[2] C. Waldschmidt and H. Meinel, "Future trends and directions in radar concerning the application for autonomous driving," in *Proc. IEEE 11th Eur. Radar Conf.*, 2014, pp. 416–419.

[3] I. Bilik, O. Longman, S. Villeval, and J. Tabrikian, "The rise of radar for autonomous vehicles: Signal processing solutions and future research directions," *IEEE Signal Process. Mag.*, vol. 36, no. 5, pp. 20–31, Sep. 2019.

[4] M. Gerstmair, A. Melzer, A. Onic, and M. Huemer, "On the safe road toward autonomous driving: Phase noise monitoring in radar sensors for functional safety compliance," *IEEE Signal Process. Mag.*, vol. 36, no. 5, pp. 60–70, Sep. 2019.

[5] M. Gerstmair, M. Gschwandtner, R. Findenig, A. Melzer, and M. Huemer, "Lego radar train — An educational workshop on radar-based advanced driver assistance systems," in *Proc. IEEE 28th Eur. Signal Process. Conf.*, 2021, pp. 1981–1985.

[6] N. Levanon, "Multifrequency complementary phase-coded radar signal," *IEE Proc. - Radar, Sonar Navigat.*, vol. 147, no. 6, pp. 276–284, 2000.

[7] B. J. Donnet and I. D. Longstaff, "Combining MIMO radar with OFDM communications," in *Proc. IEEE Eur. Radar Conf.*, 2006, pp. 37–40.

[8] C. Sturm, E. Pancera, T. Zwick, and W. Wiesbeck, "A novel approach to OFDM radar processing," in *Proc. IEEE Radar Conf.*, 2009, pp. 1–4.

[9] D. Garmatyuk, J. Schuerger, Y. T. Morton, K. Binns, M. Durbin, and J. Kimani, "Feasibility study of a multi-carrier dual-use imaging radar and communication system," in *Proc. Eur. Radar Conf.*, 2007, pp. 194–197.

[10] C. Sturm, T. Zwick, and W. Wiesbeck, "An OFDM system concept for joint radar and communications operations," in *Proc. IEEE 69th Veh. Technol. Conf.*, 2009, pp. 1–5.

[11] M. Braun, C. Sturm, A. Niethammer, and F. K. Jondral, "Parametrization of joint OFDM-based radar and communication systems for vehicular applications," in *Proc. IEEE 20th Int. Symp. Pers., Indoor, Mobile Radio Commun.*, 2009, pp. 3020–3024.

[12] O. Lang, A. Onic, C. Schmid, R. Feger, and M. Huemer, "Reducing hardware requirements and computational effort for automotive OFDM radar systems," in *Proc. IEEE 54th Asilomar Conf. Signals, Syst., Comput.*, 2020, pp. 1563–1567.

[13] G. Hakobyan and B. Yang, "A novel inter-carrier-interference free signal processing scheme for OFDM radar," *IEEE Trans. Veh. Technol.*, vol. 67, no. 6, pp. 5158–5167, Jun. 2018.

[14] C. Sturm, T. Zwick, W. Wiesbeck, and M. Braun, "Performance verification of symbol-based OFDM radar processing," in *Proc. IEEE Radar Conf.*, 2010, pp. 60–63.

[15] Y. L. Sit and T. Zwick, "Automotive MIMO OFDM radar: Subcarrier allocation techniques for multiple-user access and DOA estimation," in *Proc. IEEE 11th Eur. Radar Conf.*, 2014, pp. 153–156.

[16] G. Hakobyan and B. Yang, "A novel OFDM-MIMO radar with non-equidistant subcarrier interleaving and compressed sensing," in *Proc. IEEE 17th Int. Radar Symp.*, 2016, pp. 1–5.

[17] Y.-H. Cao and X.-G. Xia, "IRCI-free MIMO-OFDM SAR using circularly shifted Zadoff–Chu sequences," *IEEE Geosci. Remote Sens. Lett.*, vol. 12, no. 5, pp. 1126–1130, May 2015.

[18] Y.-H. Cao, X.-G. Xia, and S.-H. Wang, "IRCI free colocated MIMO radar based on sufficient cyclic prefix OFDM waveforms," *IEEE Trans. Aerosp. Electron. Syst.*, vol. 51, no. 3, pp. 2107–2120, Jul. 2015.

[19] X.-G. Xia, T. Zhang, and L. Kong, "MIMO OFDM radar IRCI free range reconstruction with sufficient cyclic prefix," *IEEE Trans. Aerosp. Electron. Syst.*, vol. 51, no. 3, pp. 2276–2293, Jul. 2015.

[20] T. Zhang, X.-G. Xia, and L. Kong, "IRCI free range reconstruction for SAR imaging with arbitrary length OFDM pulse," *IEEE Trans. Signal Process.*, vol. 62, no. 18, pp. 4748–4759, Sep. 2014.

[21] T. Zhang and X.-G. Xia, "OFDM synthetic aperture radar imaging with sufficient cyclic prefix," *IEEE Trans. Geosci. Remote Sens.*, vol. 53, no. 1, pp. 394–404, Jan. 2015.

[22] C. Knill, F. Embacher, B. Schweizer, S. Stephany, and C. Waldschmidt, "Coded OFDM waveforms for MIMO radars," *IEEE Trans. Veh. Technol.*, vol. 70, no. 9, pp. 8769–8780, Sep. 2021.

[23] J. Suh, J. Lee, G.-T. Gil, and S. Hong, "Time-and-frequency hybrid multiplexing for flexible ambiguity controls of DFT-coded MIMO OFDM radar," *IEEE Access*, vol. 9, pp. 137793–137808, 2021.

[24] C. Sturm, Y. L. Sit, M. Braun, and T. Zwick, "Spectrally interleaved multi-carrier signals for radar network applications and multi-input multi-output radar," *IET Radar, Sonar Navig.*, vol. 7, no. 3, pp. 261–269, 2013.

[25] C. Knill, F. Roos, B. Schweizer, D. Schindler, and C. Waldschmidt, "Random multiplexing for an MIMO-OFDM radar with compressed sensing-based reconstruction," *IEEE Microw. Wireless Compon. Lett.*, vol. 29, no. 4, pp. 300–302, Apr. 2019.

[26] G. Hakobyan and B. Yang, "A novel OFDM-MIMO radar with non-equidistant dynamic subcarrier interleaving," in *Proc. IEEE Eur. Radar Conf.*, 2016, pp. 45–48.

[27] R. van Nee and R. Prasad, *OFDM for Wireless Multimedia Communications, Ser. Artech House Universal Personal Communications Library*. Norwood, MA, USA: Artech House, 2000.

[28] S. Saponara and B. Neri, "Radar sensor signal acquisition and multidimensional FFT processing for surveillance applications in transport systems," *IEEE Trans. Instrum. Meas.*, vol. 66, no. 4, pp. 604–615, Apr. 2017.

[29] S. M. Patole, M. Torlak, D. Wang, and M. Ali, "Automotive radars: A review of signal processing techniques," *IEEE Signal Process. Mag.*, vol. 34, no. 2, pp. 22–35, Mar. 2017.

[30] M. Salehi and J. Proakis, *Digital Communications*, vol. 31. New York, NY, USA: McGraw-Hill Educ., 2007.

[31] C. Hofbauer, "Design and analysis of unique word OFDM," Ph.D. dissertation, Inst. Networked Embedded Syst., Alpen-Adria-Univ. Klagenfurt, Austria, 2016. [Online]. Available: https://permalink.obvsg.at/UKL/AC12608830

[32] M. K. Samimi and T. S. Rappaport, "Statistical channel model with multi-frequency and arbitrary antenna beamwidth for millimeter-wave outdoor communications," in *Proc. IEEE Globecom Workshops*, 2015, pp. 1–7.

[33] M. K. Samimi and T. S. Rappaport, "3-D millimeter-wave statistical channel model for 5G wireless system design," *IEEE Trans. Microw. Theory Tech.*, vol. 64, no. 7, pp. 2207–2225, Jul. 2016.

[34] N. Wireless, "Open source downloadable 5G channel simulator software," 2017. Accessed: Aug. 2020. [Online]. Available: http://bit.ly/1WNPpDX

[35] M. K. Samimi, S. Sun, and T. S. Rappaport, "MIMO channel modeling and capacity analysis for 5G millimeter-wave wireless systems," in *Proc. IEEE 10th Eur. Conf. Antennas Propag.*, 2016, pp. 1–5.

[36] A. Forenza, D. J. Love, and R. W. Heath, "Simplified spatial correlation models for clustered MIMO channels with different array configurations," *IEEE Trans. Veh. Technol.*, vol. 56, no. 4, pp. 1924–1934, Jul. 2007.

[37] H.-G. Yeh, "New space-frequency conjugate two-path transmission OFDM systems," in *Proc. IEEE Int. Conf. Comp., Netw. Commun.*, 2018, pp. 486–490.

[38] D. Agrawal, V. Tarokh, A. Naguib, and N. Seshadri, "Space-time coded OFDM for high data-rate wireless communication over wideband channels," in *Proc. IEEE 48th Veh. Technol. Conf.*, 1998, vol. 3, pp. 2232–2236.

[39] V. Vakilian, J. Frigon, and S. Roy, "Space-frequency block code for MIMO-OFDM communication systems with reconfigurable antennas," in *Proc. IEEE Glob. Commun. Conf.*, 2013, pp. 4221–4225.

[40] F. Uysal, "Phase-coded FMCW automotive radar: System design and interference mitigation," *IEEE Trans. Veh. Technol.*, vol. 69, no. 1, pp. 270–281, Jan. 2020.

[41] M. Huemer and O. Lang, "On component-wise conditionally unbiased linear Bayesian estimation," in *Proc. IEEE 48th Asilomar Conf. Signals, Syst., Comput.*, 2014, pp. 879–885.

[42] C. Hofbauer, W. Haselmayr, H.-P. Bernhard, and M. Huemer, "Impact of a carrier frequency offset on unique word OFDM," in *Proc. IEEE 31st Annu. Int. Symp. Pers., Indoor Mobile Radio Commun.*, London, U.K., 2020, pp. 1–7.

[43] C. Hofbauer, W. Haselmayr, H.-P. Bernhard, and M. Huemer, "On the inclusion and utilization of pilot tones in unique word OFDM," *IEEE Trans. Signal Process.*, vol. 68, pp. 5504–5518, 2020.

[44] F. Classen and H. Meyr, "Frequency synchronization algorithms for OFDM systems suitable for communication over frequency selective fading channels," in *Proc. IEEE Veh. Technol. Conf.*, 1994, pp. 1655–1659.
[45] M. Huemer, J. Hausner, and H. Witschnig, "Simulation based optimization of phase tracking algorithms for IEEE 802.11 a and Hiperlan/2 like OFDM systems," in *Proc. World Multiconf. Systemics, Cybern. Informat.*, 2002, pp. 225–229.
[46] S. M. Kay, *Fundamentals of Statistical Signal Processing: Estimation Theory*, vol. 1. Hoboken, NJ, USA: Prentice Hall, 1993.
[47] O. Lang, "Knowledge-aided methods in estimation theory and adaptive filtering," Ph.D. dissertation, Ins. Signal Process., Johannes Kepler Univ. Linz, Austria, 2018.
[48] M. Huemer, A. Onic, and C. Hofbauer, "Classical and Bayesian linear data estimators for unique word OFDM," *IEEE Trans. Signal Process.*, vol. 59, no. 12, pp. 6073–6085, Dec. 2011.
[49] *IEEE Computer Society LAN/MAN Standards Committee, Part 11: Wireless LAN medium access control (MAC) and physical layer (PHY) specifications. High-speed physical layer in the 5GHz band*. IEEE Standard 802.11a-1999 (R2003). (Supplement to IEEE Standard 802. 11-1999).
[50] S. Allpress, C. Luschi, and S. Felix, "Exact and approximated expressions of the log-likelihood ratio for 16-QAM signals," in *Proc. IEEE 38th Asilomar Conf. Signals, Syst., Comput.*, vol. 1, 2004, pp. 794–798.
[51] W. Haselmayr, O. Lang, A. Springer, and M. Huemer, "Does vector gaussian approximation after LMMSE filtering improve the LLR quality," *IEEE Signal Process. Lett.*, vol. 24, no. 11, pp. 1676–1680, Nov. 2017.
[52] O. Lang, M. Huemer, and C. Hofbauer, "On the log-likelihood ratio evaluation of CWCU linear and widely linear MMSE data estimators," in *Proc. IEEE 50th Asilomar Conf. Signals, Syst., Comput*., 2016, pp. 633–637.
[53] W. Zhang and M. J. Miller, "Baseband equivalents in digital communication system simulation," *IEEE Trans. Educ.*, vol. 35, no. 4, pp. 376–382, Nov. 1992.

Oliver Lang (Member, IEEE) received the bachelor's degree in electrical engineering and information technology, the master's degree in microelectronics from the Vienna University of Technology, Vienna, Austria, in 2011 and 2014, respectively, and the Ph.D. degree from Johannes Kepler University (JKU), Linz, Austria, in 2018. From 2014 to 2018, he was a Member of the Institute of Signal Processing with JKU. From 2018 to 2019, he was with DICE GmbH in Linz, which was a Subsidiary Company of Infineon Austria GmbH. During this period, he worked on automotive radar MMICs and systems. Since March 2019, he has been a University Assistant with Ph.D. with the Institute of Signal Processing, JKU. He is main inventor of several patents and patent applications in the field of automotive radar systems and main author of several publications in the field of estimation theory and adaptive filtering.

Christian Hofbauer (Member, IEEE) received the master's degree in hardware/software systems engineering from the University of Applied Sciences Upper Austria, Hagenberg, Austria, and the Ph.D. degree in information technology from Klagenfurt University, Klagenfurt, Austria. He is a Senior Scientist with the Wireless Communications Group, Silicon Austria Labs. His main research interests include wireless communication systems, adaptive and statistical signal processing and system architectures for mobile devices. He is a Member of the IEEE Signal Processing Society and the German Society of Information (ITG). Together with his colleagues, he was the recipient of the German EEEfCOM Innovation award for the development of the Unique Word OFDM signaling scheme in 2010.

Reinhard Feger was born in Kufstein, Austria, in 1980. He received the Dipl.-Ing. (M.Sc.) degree in mechatronics and the Dr. Techn. (Ph.D.) degree in mechatronics from Johannes Kepler University Linz, Linz, Austria, in 2005 and 2010, respectively. In 2005, he joined the Institute for Communications and Information Engineering, Johannes Kepler University Linz, as a Research Assistant. In 2007, he became a Member of the Christian Doppler Laboratory for Integrated Radar Sensors, Johannes Kepler University Linz. He is currently an Associate Professor with the Institute for Communications Engineering and RF-Systems, Johannes Kepler University Linz. His research interests include radar signal processing, and also radar system design for industrial and automotive radar sensors. Dr. Feger was the recipient of the 2011 Microwave Prize and the 2011 German Microwave Conference Best Paper Award. In 2012, he also was the recipient of the Best Measurement Paper Prize at the European Conference on Antennas and Propagation.

Mario Huemer (Senior Member, IEEE) received the Dipl.-Ing. and Dr. Techn. degrees from Johannes Kepler University (JKU), Linz, Austria, in 1996 and 1999, respectively. After holding positions in industry and academia, he became an Associate Professor with the University of Erlangen–Nuremberg, Erlangen, Germany, from 2004 to 2007, and a Full Professor with Klagenfurt University, Klagenfurt, Austria, from 2007 to 2013. Since September 2013, he has been heading the Institute of Signal Processing, JKU Linz as a Full Professor, and since 2017, he has been the Co-Head of the Christian Doppler Laboratory for Digitally Assisted RF Transceivers for Future Mobile Communications. His research interests include statistical and adaptive signal processing, signal processing architectures, and also mixed signal processing with applications in information and communications engineering, radio frequency transceivers for communications and radar, sensor, and biomedical signal processing. He was the recipient of the dissertation awards of the German Society of Information Technology (ITG) and the Austrian Society of Information and Communications Technology (GIT), respectively, the Austrian Kardinal Innitzer Award in Natural Sciences, and the German ITG Award.